Detailed analysis of the silicon surface under low-energy oxygen bombardment at atomic resolution

Takashi Yamazaki,* Yasutoshi Kotaka, Tsukasa Itani, Kazutoshi Yamazaki, and Yuji Kataoka

Device & Materials Laboratories, Fujitsu Laboratories Ltd., Atsugi 243-0197, Japan

(Received 3 January 2012; revised manuscript received 10 June 2012; published 21 August 2012)

A detailed analysis of the amorphous-SiO_2/crystalline-Si(011) interface formed by low-energy oxygen bombardment is performed by high-resolution Rutherford backscattering spectroscopy and spherical aberration-corrected scanning transmission electron microscopy (STEM). The atomic level analyses indicated a few nanometers of displaced Si atoms layer immediately below the synthetic SiO_2 layer. A comparison between intensities of the high-angle annular dark field (HAADF) STEM image and the simultaneously acquired high-angle bright-field (HABF) STEM image shows that both intensities decreased at the existing layer of displaced Si atoms, and the relationship between these intensities cannot be explained by conventional image formation mechanisms. From detailed investigations using STEM imaging simulations, the HAADF STEM and HABF STEM images, which were simulated based on a realistic model, revealed the random distribution of a crystalline material and amorphous material at the interface; and this result agrees well with experimental results.

DOI: 10.1103/PhysRevB.86.085438 PACS number(s): 68.35.−p, 61.72.U−, 68.37.−d, 68.49.−h

I. INTRODUCTION

Oxygen bombardment is a well-established technique for the introduction of oxygen into a target surface and the conversion of a surface to an oxide. Most of the studies regarding oxidation techniques have been done in the field of Si-based semiconductor manufacturing from the perspective of an ultrathin gate oxide layer[1–7] and a silicon on insulator (SOI) substrate.[8,9] The oxidation technique has also been applied to secondary ion mass spectrometry (SIMS), which measures dopant depth profiles for the formation of ultrashallow junctions. In SIMS, the formation of an oxide layer at the bombarded surface causes high yields of positive secondary ions and provides low detection limits in the parts per billion range. However, the surface oxidation of the sputter eroded sample leads to a degradation of depth resolutions and artifacts that mislead interpretations of the measured depth profiles.[10–21] The thickness of the oxide layer and the structure immediately below the oxide layer are highly sensitive factors in understanding these effects.

Several phenomenological models have been proposed to study the oxidation process,[9,22–25] and various experimental techniques have been used to observe the altered structures.[1–5,14,15,26–35] For the SOI technology, transmission electron microscopy (TEM),[26,27] Rutherford backscattering spectroscopy (RBS),[28] and SIMS[33,34] have exhibited SOI micro-structures that are formed by oxygen implantation and a redistribution of the oxygen implanted into the Si substrate for high-energy oxygen bombardment (from several tens of keV to 200 keV). Low-energy oxygen bombardment has also been examined for the formation of ultrathin gate oxides and for the SIMS depth profiling of ultrashallow implants. X-ray photoelectron spectroscopy (XPS) and TEM showed that the normal incidence of 40–200 eV oxygen ions produce an oxide layer on Si(100), saturating at 4-nm thickness with a sharp oxide interface.[6] RBS quantified the influence of oxygen bombardment parameters on the alteration of the silicon surface. A linear dependence of the oxide thickness on oxygen energy was obtained in the energy range of 3–40 keV (per oxygen ion).[14] The SiO_2 thickness was determined mainly by the oxygen range distribution in SiO_2 and was actually close to the sum of the projected range and the range straggling of the implanted oxygen ions in SiO_2, $R_p + \Delta R_p$.[14,30] The SiO_2 layer was followed by a heavily damaged layer.[14,15,29,31] However, the technology of ultrathin oxide layers (in particular for SIMS), requires more intensive investigations into the SiO_2/Si interface structures for a steeper interface and a higher depth resolution. Recently, advanced analytical techniques, such as high-resolution Rutherford backscattering spectrometry (HRBS) and spherical aberration (C_s)-corrected scanning transmission electron microscopy (STEM) enable investigations into the structural and compositional changes with high resolutions at the atomic level.

The application of STEM as an evaluation tool has attracted worldwide attention. STEM, or Z-contrast imaging, saw major development in the 1990s. The image intensity of a high-angle annular dark-field (HAADF) STEM image, which is obtained by setting the detector angle to a sufficiently high value for detecting electrons scattered by thermal diffuse scattering (TDS), is highly dependent on the atomic number. Furthermore, projected atomic columns are identified by bright spots and are independent of the defocus value of probe-forming lens and sample thickness, which are unlike conventional high-resolution TEM images.[36–40] However, recent detailed studies report the need of theoretical quantitative and qualitative analysis.[41–43] The development of the C_s corrector, which was first commercially manufactured by Haider *et al.*, was a big breakthrough in the field of electron microscopy.[44–47] A high-quality image having high signal-to-noise ratio (SNR) is obtained by the use of an incident probe with a very large electric current. In addition, structural and compositional analyses and arguments of the electronic state are enabled by making a comparison between a STEM image and electron energy loss spectroscopy (EELS) mapping, which is acquired by a fine probe with a subnanometer scale.[48,49]

The STEM method has been used for a long time to analyze the interface structure of electronic devices. Nakanishi *et al.*[50] performed a detailed structural analysis of the SiO_2/Si interface by systematic analysis consisting of image deconvolution processing and fitting with dynamical simulation. Their results showed that the formation of crystalline SiO_2 at the oxidation

 ©2012 American Physical Society

front does not appear to be essential for layer-by-layer oxidation to occur. In addition, Yu *et al.*[51] measured the induced strain of the interface of SiO_2/Si by using the annular dark-field (ADF) STEM image, which is obtained by a detection angle that is set to be small enough to allow an interference effect to be taken in positively. However, there are few reports regarding the analysis of the interface structure using a physical and realistic interface model. Therefore, investigations into the roughness, strain, and damage layer in the interface region have almost always been analyzed with an extremely simple model, even for quantitative analyses. The reasons cited for the lack of detailed structural information of damage layer and the difficulties associated with these analyses include the simulation of an actual interface model using a huge supercell and the analysis of amorphous films using the STEM method.

In this study, silicon oxide layers were formed on *p*-type Si(100) wafers at low O_2^+ energies, 180 eV–5 keV (90 eV–2.5 keV per oxygen ion), and at normal incidence. The dependence of the oxide layer thickness and the SiO_2/Si interface structure on the O_2^+ bombardment energy was explored using HRBS, C_s-corrected STEM, and EELS. Furthermore, amorphous/crystal interfaces that were formed due to oxygen bombardment were analyzed using systematic dynamical simulations and simultaneously obtained HAADF STEM and high-angle bright-field (HABF) STEM images.[52] The aim of this study was to explore in more detail the structure of the Si surface, which was altered by low-energy oxygen bombardment, and to better understand the formation of ultrathin oxide layers under oxygen bombardment.

II. EXPERIMENTAL PROCEDURE

The oxygen bombardment was performed using a commercial SIMS instrument, ATOMIKA 4500, which was equipped with a floating ion gun that delivers O_2^+ ions to the sample surface as low as 150 eV. The O_2^+ ions were rastered over an area of 1000×1000 μm at an impact angle of 0° (at normal incidence). The beam currents were 20 (at 180 eV)–100 (at 5 keV) nA. Detailed oxygen bombardment energies were set to 180 eV, 500 eV, 1 keV, and 3 keV, respectively. The Si^+ and O^+ signals from the bombarded surface were monitored, and the bombardment was stopped after the signals reached a stationary state. In each case, the oxygen dose was sufficiently high to form a continuous SiO_2 layer, i.e., above a dose of 5×10^{17} O_2^+/cm^2. Samples that show the most detailed analysis results are those of 180 eV O_2^+ bombardment and 3 keV O_2^+ bombardment. These are hereafter referred to as "sample #1" and "sample #2," respectively.

The HRBS system used, HRBS 500, enabled us to obtain depth profiles with a depth resolution of a few tenths of a nanometer. In the instrument, ions scattered from the specimen are energy-analyzed by a magnetic spectrometer and detected by a microchannel-plate position-sensitive detector placed at the focal plane of the spectrometer. This allows the measurement of the energy spectrum without sweeping the magnetic field. The HRBS spectra were measured using a 300 keV He^+ beam. The [101] channel (the angle of incidence θ was 45° with respect to the surface normal) was used for all the layers to reduce the signals from the Si substrate. The scattering angle was varied between 52° and 70° in accordance with the oxide thickness for separating the signals of Si and O with high resolution.

The STEM observation was performed using a JEM-2100F TEM/STEM, which was operated at 200 keV and equipped with a C_s corrector. In the present experiment, a HAADF STEM image and a HABF STEM image were simultaneously observed. The semiangle of the incident probe and range of the ADF detector were precisely determined from microdiffraction[53] to be 20 mrad and 70–185 mrad, respectively. The collection angle of the bright-field (BF) detector was estimated to be 18 mrad. In C_s-corrected HAADF STEM images, the effect of defocus spread due to the chromatic aberration coefficient (C_c coefficient) and energy distribution of the incident beam cannot be ignored. The C_c coefficient was measured by a method suggested by Kuramochi *et al.*[54] and was found to have a value of 1.72 mm. The standard deviation of the incident energy distribution was 1.0 eV, as measured from the shape of the zero-loss spectrum of EELS. Sample thicknesses were measured by zero-loss spectrum of EELS using the log-ratio method.[55,56] The observed areas in all samples were selected such that they were about 30 nm thick.

In the present study, the algorithm used for the calculation of the STEM image is a dynamical calculation suggested by Watanabe *et al.*[57] and then expanded by Yamazaki *et al.*[58] This algorithm calculates a STEM image described by TDS electrons to consider two kinds of optical potentials. In addition, by direct calculation of the elastic scattered electrons detected by the BF detector, a BF STEM image can be simultaneously calculated. In order to calculate the STEM image of an amorphous material, a one-beam approximation suggested by Yamazaki *et al.*[59] is used. This approximation is valid for estimating the average intensity of amorphous material, although the granular contrast of the STEM image cannot be calculated.

III. RESULTS AND DISCUSSION

A. Structural model of damage layer below the synthetic SiO_2 layer

Figure 1 shows the HRBS spectra observed for the Si(100) wafers bombarded with 250 and 500 eV O_2^+ at normal incidence. Both spectra clearly show the formation of surface oxide layers. The inset in the upper left of the figure indicates the depth profiles of oxygen and silicon converted from the HRBS spectrum of 500 eV O_2^+ bombardment. The energy scales in the HRBS spectra were converted to depth scales using the stopping powers of SiO_2 (2.20 g/cm^3) and Si (2.33 g/cm^3). The conversion was done using the simulation software "Analysis IB," which was developed by Kobe Steel, Ltd., using Yang's empirical formula for energy loss straggling.[60]

Assuming that the SiO_2/Si interface was at a half of the maximum oxygen intensity, the thicknesses of the oxidized layers were determined from the depth profiles of oxygen. In Fig. 2, the dependence of the silicon oxide thickness on the O_2^+ bombardment energy is depicted together with the result of the transport of ions in matter (TRIM) calculation, $R_p + \Delta R_p$. This was done using the stopping power version "SRIM-2008." The silicon oxide thickness decreases with

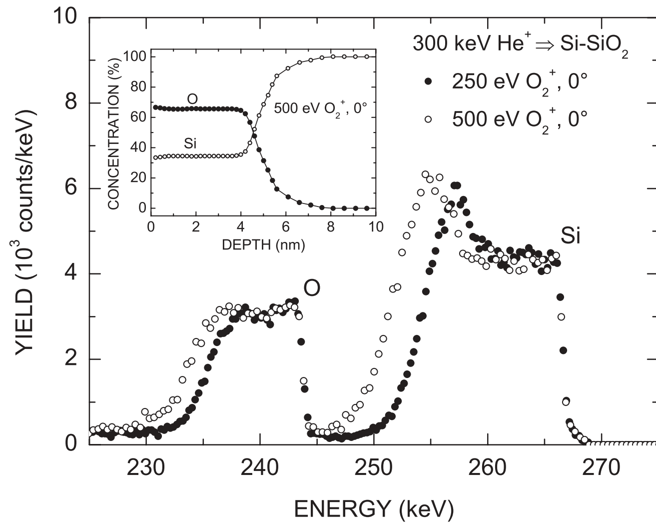

FIG. 1. HRBS spectra for the Si(100) wafers bombarded with 250 and 500 eV O_2^+ at normal incidence. Inset: Depth profiles of oxygen and silicon converted from the HRBS spectrum of 500 eV O_2^+ bombardment.

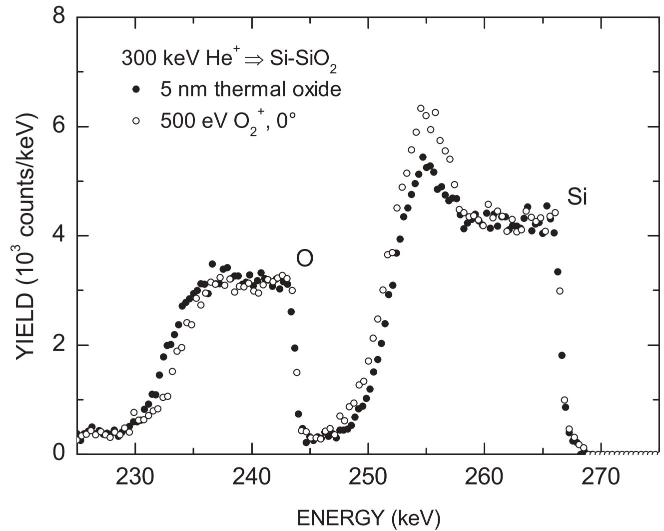

FIG. 3. HRBS spectra for the silicon oxide layers of the same thickness, 5.0 nm, formed by O_2^+ bombardment and by the thermally grown process.

decreasing O_2^+ bombardment energy and is saturated at about 4 nm. The results obtained from the HRBS measurements are in agreement with those of previously published works.[3,11,14]

Figure 1 also indicates the possibility of disordered Si immediately below the oxide layer. Figure 3 is a comparison of the HRBS spectra for the silicon oxide layers of the same thickness, 5.0 nm, formed on Si(100) by 500 eV O_2^+ bombardment, and by the thermally grown process at 900 °C in dry oxygen. The two sets of HRBS spectra exhibit a slight difference in the silicon signals near the SiO_2/Si interface. The signals for the Si wafer bombarded with O_2^+ are greater than those covered with the thermal oxide. The figure suggests that even if the thickness of the oxide layer is the same, oxygen bombardment generates Si that is much more disordered than that in the case of thermal oxidation.

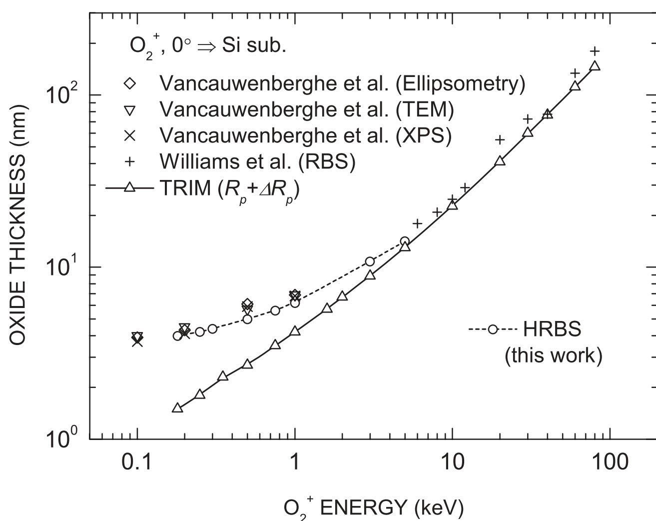

FIG. 2. Dependence of the silicon oxide thickness on O_2^+ bombardment energy, compiled from various sources.[3,11,14]

The areal densities of silicon and oxygen were calculated from the HRBS spectra for different thicknesses of SiO_2 layers formed under various conditions of O_2^+ bombardment and thermal oxidation. In Fig. 4, the areal density of oxygen is plotted versus that of silicon for both O_2^+ bombardment and thermal oxidation. The dataset for the O_2^+ bombardment was obtained from the HRBS spectra measured for 250, 500, 750 eV, and 1 keV, and that for the thermal oxidation was obtained from the HRBS spectra for the seven thermal oxide layers of different thicknesses (0.5, 0.8, 1.0, 1.5, 1.8, 2.5, and 5.0 nm), grown on Si(100) wafers in dry oxygen at 700–950 °C. All of the HRBS spectra were measured at a scattering angle

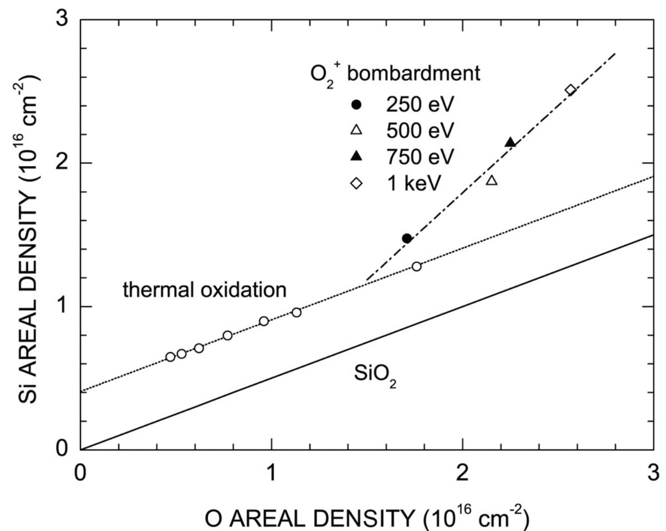

FIG. 4. Areal density of oxygen and silicon for the oxide layers on Si(100) formed under various conditions of O_2^+ bombardment and thermal oxidation. The dataset for the thermal oxidation obtained from seven thermal oxides of different thickness, 0.5, 0.8, 1.0, 1.5, 1.8, 2.5, and 5.0 nm (by ellipsometry), grown on Si(100) wafers in dry oxygen at 700–950 °C. The oxygen areal density is proportional to the thickness of the SiO_2 layer.

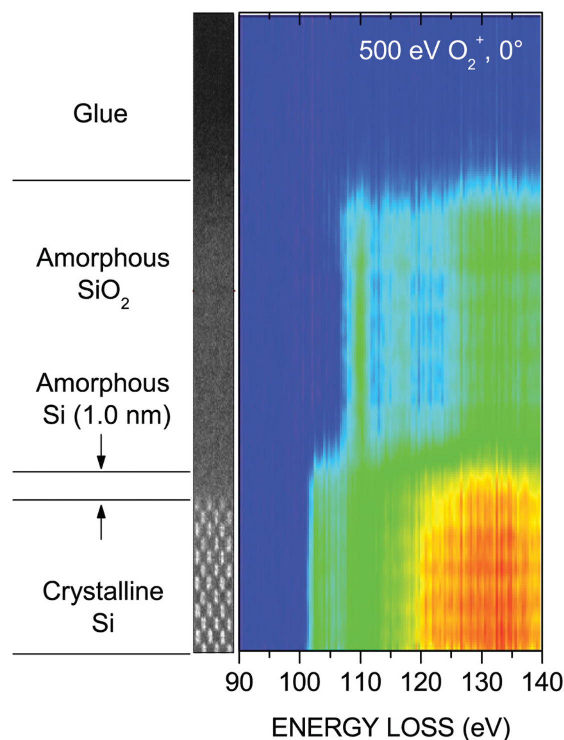

FIG. 5. (Color online) STEM image and EELS spectra for 500 eV O_2^+ bombardment at normal incidence. The image on the right side is an EELS map composed of the measured spectra. Examples of the measured spectra are depicted on the EELS map.

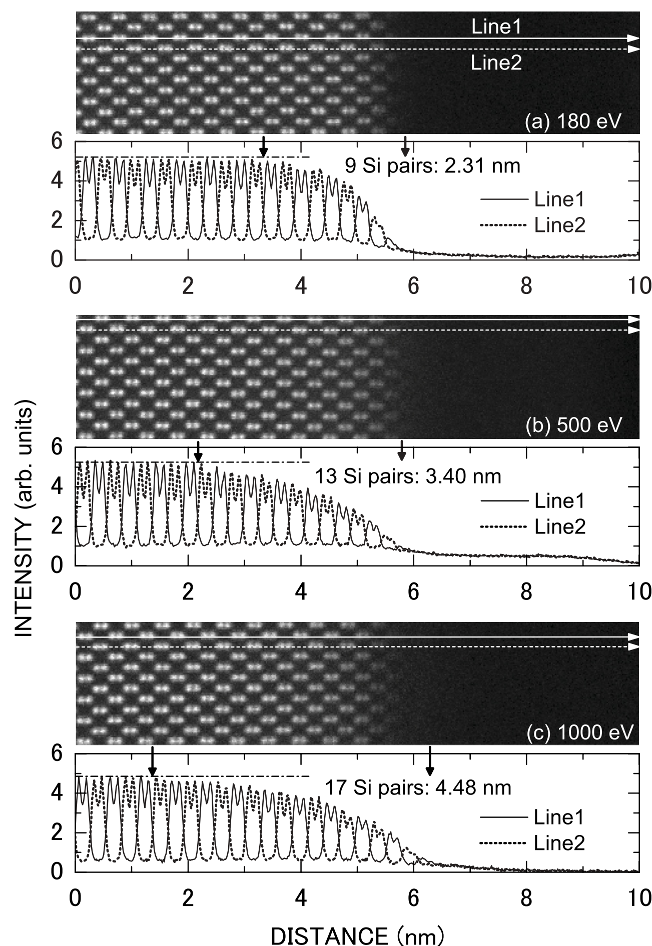

FIG. 6. Cross-sectional HAADF STEM images and line profiles of the intensities obtained from the O_2^+ bombarded areas. The O_2^+ bombardment was performed at (a) 180 eV, (b) 500 eV, and (c) 1 keV and at normal incidence.

of 57° to prevent variations in the intrinsic surface peak in the HRBS spectra. The solid line represents the relation of an ideal interface composed of a perfect Si single crystal and stoichiometric SiO_2. The dataset for the dry oxidation is fitted with a straight line of the same slope as the stoichiometric SiO_2. The intercept on the vertical axis suggests the amount of excess Si in the interface region between the Si single crystal and the SiO_2 layer. The plot for the O_2^+ bombardment exhibits a slope with a gradient that is slightly higher than one-half, indicating that the oxide is stoichiometric SiO_2. The steeper slope implies that the excess Si, i.e., the disordered Si, increases with increasing O_2^+ bombardment energy.

Figure 5 is an example of the C_s-corrected STEM-EELS results for the Si surface altered by the O_2^+ bombardment. The STEM image and the corresponding EELS spectra are along the [100] direction for 500 eV O_2^+ bombardment at normal incidence. The image on the right side is an EELS map composed of the measured spectra and shows the relationship between the loss energy and the measured point. Representatives of the measured spectra are depicted on the EELS map. The figure suggests that a 1.0-nm layer of heavily disordered Si, i.e., amorphous Si (*a*-Si), was formed immediately below the synthetic SiO_2 layer. The STEM-EELS analyses for 180 eV and 1 keV O_2^+ bombardment indicated *a*-Si layers of thickness 0.5 and 1.6 nm, respectively.

Figure 6 shows the cross-sectional HAADF STEM images obtained from the O_2^+ bombarded areas. In the images, the 0.136-nm dumbbells are clearly resolved. The line profiles of the intensities are depicted with the STEM images. These images and line profiles indicate that Si atoms were displaced over a distance of 9, 13, and 17 Si pairs, i.e., a lattice distortion of 2.31, 3.40, and 4.48 nm, respectively, below the amorphous region with the O_2^+ bombardment at 180, 500 eV, and 1.0 keV, respectively.

The STEM-EELS analyses of the chemical state and the HAADF STEM observation of the lattice structure imply that a thin layer of heavily disordered Si atoms, i.e., the *a*-Si layer, follows the SiO_2 layer, and the displaced Si atoms gradually change from being amorphous to being a single crystal over a distance of 2.8 to 4.6 times the *a*-Si layer thickness, depending on the O_2^+ bombardment energy. In Fig. 4, the *a*-Si layer generated by the O_2^+ bombardment is close to the thickness realized by thermal oxidation at an oxygen areal density of about 1.5×10^{16} cm^{-2}, which was estimated at about 150 eV. However, the single crystal is damaged over a distance that is more than five times that of the *a*-Si layer by the oxygen bombardment.

B. Detailed structural analysis of disordered layer by STEM imaging

The considered model of the SiO_2/Si interface formed by low-energy oxygen bombardment is schematically shown in

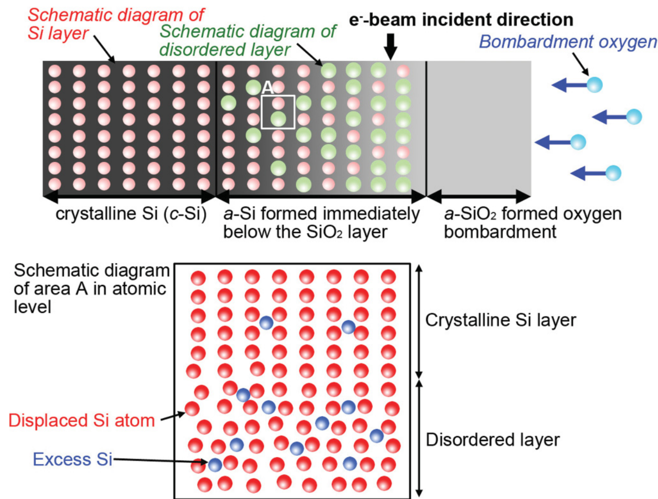

FIG. 7. (Color online) Schematic diagram of interface below the synthetic SiO_2 layer generated by the low-energy oxygen bombardment.

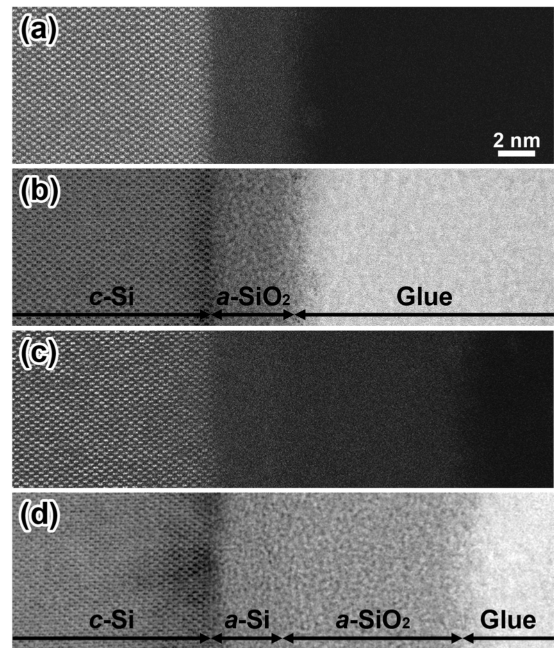

FIG. 8. (a) HAADF STEM image and (b) HABF STEM image of the SiO_2/Si interface of the O_2^+ bombardment sample at 180 eV (sample #1). (b) HAADF STEM image and (c) HABF STEM image of the SiO_2/Si interface of the O_2^+ bombardment sample at 3 keV (sample #2).

Fig. 7 as a summary of the analysis of the above subsection. However, the ion beam analysis enables us to measure the number of disordered atoms but depiction of disordering is limited by its spatial resolution. Therefore, although it is possible to measure the amorphous layer thickness of the sample irradiated by high-energy O_2^+ ions, it is hard to precisely evaluate disordered layer of the sample irradiated by low-energy O_2^+ ions. Therefore, in order to clearly understand the structure altered by low-energy ion bombardment below 1 keV, the detailed structural analysis of that interface is performed by using HAADF STEM images and HABF STEM images with atomic resolution. The cross-sectional STEM images of samples #1 and #2 are shown in Fig. 8. Figures 8(a) and 8(b) are the HAADF STEM image and HABF STEM image of sample #1, respectively. Figures 8(c) and 8(d) are the HAADF STEM image and HABF STEM image of sample #2, respectively. We define the amorphous/crystalline interface position where an atomic column can be seen in the HAADF STEM image, and the positions of the displayed images are adjusted to maintain those interface positions. For the characteristics of the crystalline region and amorphous region to be easily seen, intensity line profiles, which average the intensities of low-magnified STEM images along the parallel direction against the interface, are displayed in Fig. 9. Figures 9(a) and 9(b) are the average intensity line profile of samples #1 and #2, respectively. According to Fig. 9(b), there is a slight difference between the average intensities. These slight intensity differences are caused by the difference of a-Si and a-SiO_2. From these results, in sample #1, the amorphous SiO_2 (a-SiO_2) exists 4.3 nm from the interface. In sample #2, the amorphous region exists up to 14.5 nm from the interface. In sample #2, a-Si comprises 3.3 nm of the 14.5-nm amorphous region from the interface; the remainder of the 14.5 nm is composed of a-SiO_2. Furthermore, the most characteristic phenomenon of these experimental results is that the intensities of both the HAADF STEM image and the HABF STEM image decrease at the interface. Generally, the intensity and/or the contrast of the HABF STEM image should increase when those of the HAADF STEM image decrease, because the HABF STEM image is a complementary image of the HAADF STEM image.[52] However, it is found that the complementarity of STEM images collapses in the region surrounded by a

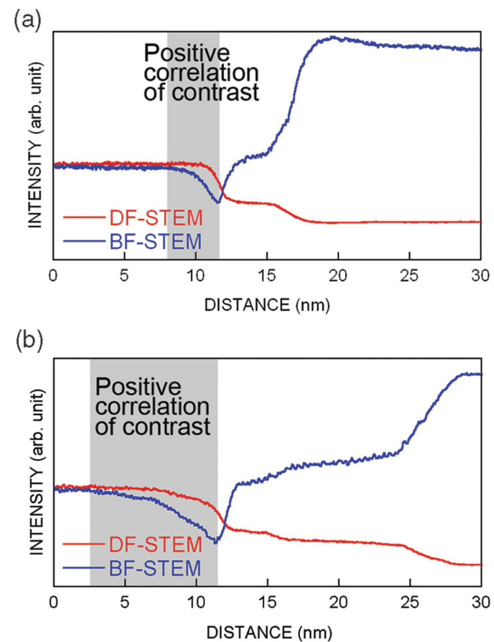

FIG. 9. (Color online) (a) Average intensity profiles of HAADF STEM image and HABF STEM image acquired at low magnification of sample #1. (b) Average intensity profiles of HAADF STEM image and HABF STEM image of sample #2 acquired at low magnification. The average intensity is obtained along the direction parallel to the interface.

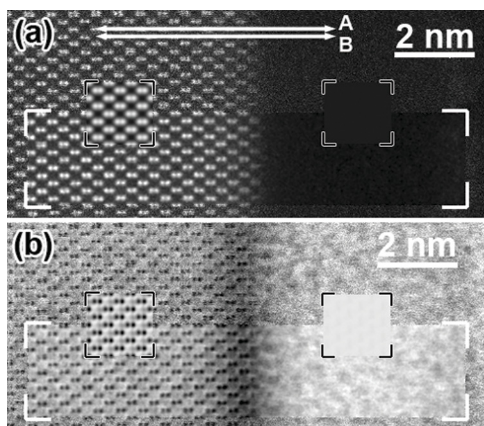

FIG. 10. (a) Enlarged HAADF STEM image and (b) enlarged HABF STEM image of sample #1. The averaged images and best matched simulated images of c-Si and a-SiO_2 are superimposed, respectively.

gray band in Figs. 9(a) and 9(b). The region in which this complementarity collapses is hereafter called the "region of positive correlation contrast" to indicate that the contrast of the HAADF STEM and of the HABF STEM images shows positive correlation.

From here, we discuss the atomic structure of the interface of a-SiO_2/c-Si based on the previous experimental results. Figures 10(a) and 10(b) display the enlarged HAADF STEM image and HABF STEM image of sample #1, respectively. The processed images (by averaged processing using translational symmetry) are superimposed onto the raw images in the area marked off by white corners.[61] The regions including the interface are analyzed by comparing the simulated image to experimental images. For the first step, we first measure various unknown experimental parameters by comparing the experimental and simulated images of the matrix region, which is separate from the interface. In the present study, the parameters sought by this analysis are the defocus value, effect of spatial incoherence, and the detector position of the BF detector. Spatial incoherence is defined as a combination of effects arising from factors such as the finite extent of the effective illumination source, instabilities, and sample drift.[56] Spatial incoherence can be modeled by convoluting the simulated HAADF STEM images with a Gaussian envelope function: The effect of spatial incoherence is expressed by the full-width half-maximum (FWHM) of the Gaussian envelope function. Because it is very difficult to directly measure these parameters in C_s-corrected STEM images, these values are precisely measured by a fitting procedure. In order to precisely estimate these parameters, a multiobjective optimization method is used. The object function of the optimization is set to the correlation coefficients between the simulated and experimental STEM images. Then, experimental parameters are determined as correlation coefficients of both HABF STEM and HAADF STEM images and are obtained for maximum values by using multiobjective Genetic Algorithm. A detailed explanation of the optimization method and the influence of the BF detector position are discussed elsewhere.[62] Therefore, the average and best-matched simulated images are superimposed in the area marked off by the black corners in Figs. 10(a) and 10(b), respectively. The results for a-SiO_2 simulated under the same condition are simultaneously shown. The intensities of the right and left atomic columns of the a-Si dumbbell structure are significantly different in the HABF STEM image. It is thought that this is because the BF detector has shifted slightly from the center of the transmitted convergent disk. In the present study, it is confirmed that we can precisely calculate the STEM image of the matrix region and the intensity ratio between the crystalline and amorphous region by determining the most suitable calculation condition using the optimization method.

To show a detailed comparison between experimental and simulated results, the averaged intensity line profiles along A and B of Fig. 10(a) are shown in Fig. 11. Figure 11(a) shows the intensity line profiles of the HAADF STEM image, and Fig. 11(b) shows the intensity line profiles of the HABF STEM image. Each intensity line profile of the experimental results is expressed by markers, and the simulated results of the matrix region are expressed by solid lines. It is confirmed that there is good agreement of both at the matrix region. Another important observation from this figure is that the position at which the contrast of the HABF STEM image is the lowest and the position at which the atomic column in HAADF STEM image cannot be detected do not correspond. The arrows within each figure show the position at which the contrast of the HABF STEM image is lowest. In Fig. 11(a), the intensity corresponding to the atomic column of the Si may be slightly more visible on the a-SiO_2 side than this arrow. This is a very important phenomenon. Temporarily, we assume that the position of the c-Si/a-SiO_2 interface is the position at which the contrast of the HABF STEM image is the lowest. Under this assumption, when the crystallization of Si increases with

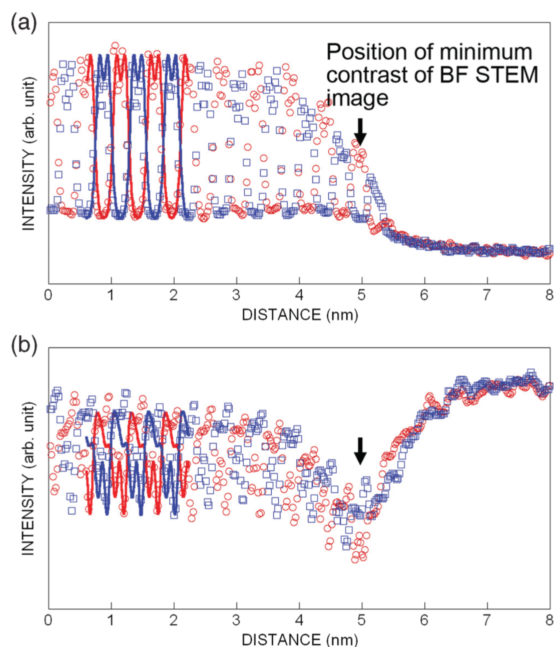

FIG. 11. (Color online) (a) Intensity line profiles of HAADF STEM image and (b) HABF STEM image along A and B lines shown in Fig. 10(a). Intensity line profiles are obtained by averaging over 10 lines. The arrows within each figure show the position at which the HABF STEM image contrast is lowest.

shifts to the c-Si side as opposed to the assumed interface, the intensity of both the HAADF STEM image and HABF STEM image simultaneously increase. Conversely, with a decrease in the crystallization of Si due to shifts to the a-SiO_2 side as opposed to the assumed interface, the intensity of the HAADF STEM image decreases, but that of the HABF STEM image increases. Such a physical phenomenon has to exist near the interface.

To explain the above phenomenon, we investigate the extent to which the a-Si, i.e., the disordered layer that is suggested at the previous subsection in detail, influences the HAADF STEM and HABF STEM images by dynamical simulation. At this stage, we assume that a-Si, whose concentration ranges from 0 to 100%, exists, and c-Si, whose concentration ranges from 100 to 0%, exists near the interface; the net concentration of c-Si and a-Si is 100%. Here, we inspect the mechanism by which a-Si mixes with c-Si. To do this, we perform calculations for some interface models for confirmation purposes. The schematic diagrams of the inspected mixture models of c-Si and a-Si are displayed in Figs. 12(a)–12(d). In these schematic diagrams, the light circles denote a-Si and the dark circles denote c-Si, respectively. These mixture models clearly show that the crystallization of Si increases with movement to the left. In the schematic model shown in Fig. 12(a), c-Si exists at the top side on the sample, and a-Si exists at the bottom side. The schematic model shown in Fig. 12(b) is the reverse model of Fig. 12(a). In other words, models A and B are results that examine the so-called top-and-bottom effect. The schematic diagram shown in Fig. 12(c) is the model for which the sample's central part is c-Si, and there are a-Si regions at the top and bottom sides. Finally, model D illustrates a model in which c-Si and a-Si layers are randomly mixed. Figure 12(e) displays the results as a plot of the relationship between the average intensities of the HAADF STEM and HABF STEM images in the unit cell and the crystallization of Si at each amorphous mixing model. It should be noted that the changes in the behavior of the average intensities of models A–C are insignificant. These results were discussed in detail by Yamazaki *et al.*[59] When an amorphous substrate that can be expressed by a one-beam approximation exists in the calculation of an HAADF STEM image, the amorphous substrate only reduces the intensity of the wave packet of the incident probe by the absorption effect, and the STEM image intensity is not changed by the specific scattering phenomenon at the amorphous substrate. Therefore, the amorphous material at the top side of the sample changes the focus distance for a crystalline part and reduces average intensity. The lower amorphous substrate of the sample reduces only the average intensity. Therefore, the STEM images of models A–C are regarded as the images simulated by different defocus values, because models A–C have equal crystallization concentration values. Generally, the average intensity of a STEM image is independent of the defocus value. Therefore, the average intensities are almost equal for each model. In addition, in these models, a change of crystallization is considered to be similar to a change of thickness. Therefore, because the complementarity of HAADF and HABF STEM images is preserved, the positive correlation contrast region shown in Fig. 9 cannot be explained by these easy models. On the other hand, it is found that the average intensities of the HAADF and HABF STEM images of model D show the positive correlation to within 0–40% of the a-Si concentration. This phenomenon can adequately explain the fact that the Si column may be more visible at the a-SiO_2 side than at the minimum contrast position of the HABF STEM image.

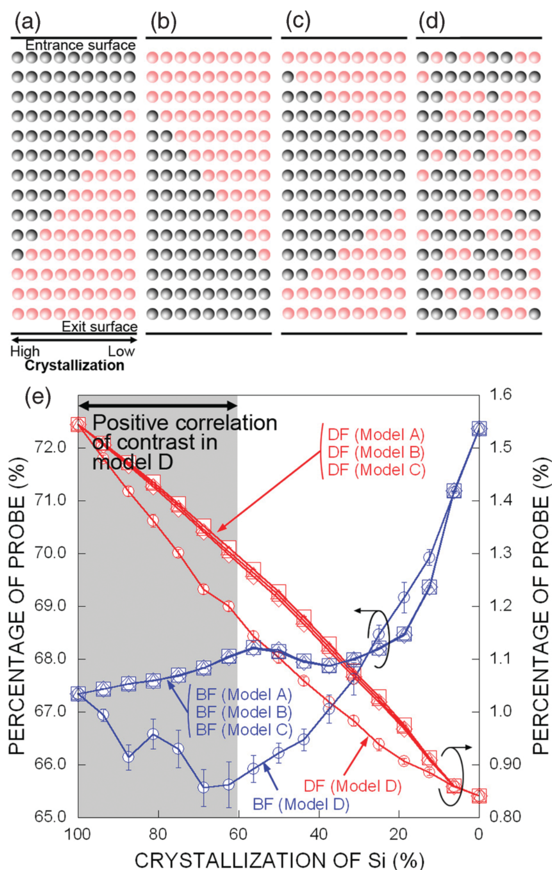

FIG. 12. (Color online) (a)–(d) Schematic diagrams of respective models used to consider the mixing of c-Si and a-Si. Solid and light circles schematically express c-Si and a-Si, respectively. (e) Relationship between average intensities of HAADF and HABF STEM images, which are simulated by using each interface model and the crystallization concentration.

In the present study, by performing a detailed examination of the interface model, it is possible to explain the contrast of the HAADF STEM and HABF STEM images at the a-SiO_2/c-Si interface. Consequently, it was found that the average intensity of the HAADF STEM image is a monotone increasing function for the crystallization of Si, without considering the structural model. Therefore, the crystallization concentration of Si is measured by making a comparison between the average intensity profiles shown in Fig. 9 and the simulated average intensity for the crystallization concentration of Si shown in Fig. 12(e). Figure 13(a) shows the HAADF STEM image simulated by a supercell that consists of a c-Si and a-Si mixing model, and the crystallization concentration measured by the above method is inserted. The gradual decrease of the intensity close to the interface is well reproduced. Figure 13(b) displays the result obtained by inserting the corresponding HABF STEM image simulated by the same supercell. Although there remain small quantitative disagreements, the validity of the

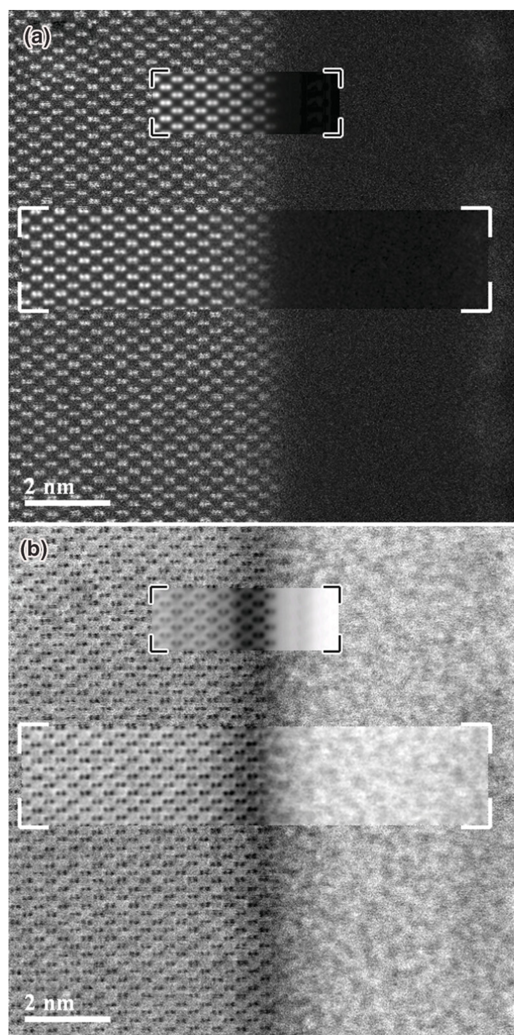

FIG. 13. (a) Enlarged HAADF STEM image and (b) enlarged HABF STEM image of sample #1. The average images and image simulated using a supercell of the random mixture model of c-Si and a-Si are superimposed, respectively. Images marked off by white corners are average processing images, and images marked off by black corners are the dynamical simulated images.

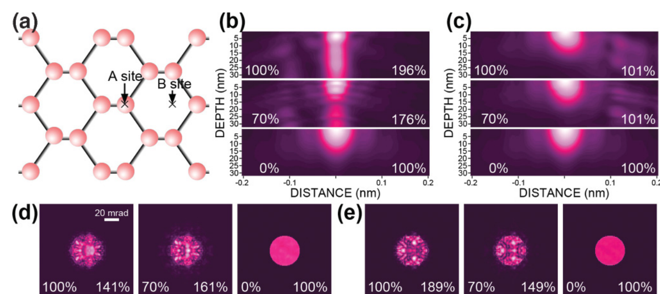

FIG. 14. (Color online) (a) Projected atomic structure of Si(011), (b) and (c) are convergent wave fields of xz plane at respective incident positions, and (d) and (e) are diffraction patterns at respective incident positions. Each diffraction pattern is calculated for a thickness of 32 nm.

present model of the interface has been verified, because the characteristic of the HABF STEM image is qualitatively well reproduced.

To investigate in detail the formation mechanism of the positive correlation for the contrast which appears due to the induction of a damaged layer, the wave field excited by a convergent electron beam and the diffraction pattern are systematically analyzed by a dynamical simulation. The calculation results are displayed in Fig. 14. Figure 14(a) shows the projected atomic structure of Si(011). We calculated the convergent wave fields and diffraction patterns when the convergent electron beam is illuminated on sites A and B, which are shown in Fig. 14(a). Figures 14(b) and 14(c) show the convergent wave fields at the xz plane; in this case, the incident beam direction is set to the z axis, and the [100]-direction is set to the x axis. Figure 14(b) shows the convergent wave fields when the convergent electron beam is illuminated on site A, and Fig. 14(c) shows the convergent wave fields when the convergent electron beam is illuminated on site B, respectively. The crystallization concentrations are given at the bottom left corner of each image. The maximum intensities that are normalized by the maximum intensity of 0% crystallization concentration are given at the bottom right corner of each image. From the results of Fig. 14(b), when the convergent electron beam is illuminated on the atomic site (A site), it is confirmed that the channeling electrons are localized at the atomic column in the case of c-Si. On the other hand, in the case of the layered structure including a-Si, the decay of channeling electrons is more remarkable than the case of c-Si because of the existence of the a-Si layer. Furthermore, the behavior of electrons which is illuminated on the intercolumn (site B) is almost the same as the behavior of a-Si without the electrons being located in neighboring atomic columns. From these results, the difference in the intensities of the convergent wave fields located on atomic column due to the site of the incident convergent electron beam and the content of the a-Si layer appears as the difference of the HAADF STEM image intensity. Therefore, it is understood that the HAADF STEM intensity is decreased by increasing the content of the a-Si layer.

For a detailed discussion of the formation mechanism of HABF STEM images, it is necessary to view the diffraction pattern for each incident beam position. The diffraction patterns when the convergent electron beams are illuminated on sites A and B are shown in Figs. 14(d) and 14(e), respectively. The percentages shown at the bottom of each image express the same information shown in Figs. 14(b) and 14(c). The intensity of the HABF STEM image gives a result that integrates the intensity of these diffraction patterns by the BF detector as a function of the incident beam position. From these results, when the convergent electron beam is illuminated on the atomic site, the intensity of the layered structure including the a-Si layer is higher than the intensity of c-Si. Therefore, from only these results, we cannot explain the positive correlation of the contrast. However, it is found that the net intensity of the layered structure including the a-Si layer is weaker than the net intensity of c-Si when the convergent electron beam is illuminated on the intercolumn site. This phenomenon can be explained as follows. In the case of c-Si, because the intercolumn site is regarded as the hollow for a fine probe made by the C_s-corrector, there is very little absorption

at the intercolumn site. On the other hand, in the case of a layered structure including the *a*-Si layer, absorption occurs due to the atoms of the *a*-Si layer, even if the incident electron beam is illuminated on the intercolumn site. Therefore, when an *a*-Si layer having an area that is several dozen percent of the overall area is included, the intensity of the wave field is significant at the atomic site, but the intensity of the wave field is weak at the intercolumn site. Because the weakness of the intensity at the intercolumn site is dominant to the HABF STEM image for a range of content of *a*-Si that demonstrates a positive contrast correlation, the average intensity of the HABF STEM image decreases. When the content of the a-Si layer further increases, the existence of *a*-Si, which originally experiences less of the localization effect at the atomic site, becomes more dominant, and the absorption becomes weak. Consequently, it was found that the intensity of the HABF STEM image, together with an increased *a*-Si content and the average intensity of the HABF STEM image becomes higher than the average intensity of *c*-Si.

IV. CONCLUSION

In conclusion, we have investigated the structure of the Si surface that is altered by low-energy O_2^+ bombardment (180 eV–3 keV) at normal incidence using HRBS, C_s-corrected STEM-EELS, and C_s-corrected STEM imaging. The HRBS and the STEM-EELS results showed that a thin layer of heavily disordered Si, i.e., an *a*-Si layer, is formed immediately below the synthetic SiO_2 layer. The HAADF STEM observations with atomic resolution showed that below the *a*-Si layer, the displaced Si atoms gradually change from being amorphous to being single crystals over a distance of a few nanometers for normal O_2^+ incidence. To show a precisely atomic structure at the interface, analysis by dynamical simulation was performed on the HAADF and HABF STEM images. In the interface region that exists immediately below the synthetic SiO_2 layer, a STEM image contrast that cannot be explained by conventional image interpretation was obtained, and this contrast decreased in both the HAADF and HABF STEM images. Construction of the interface model suggested by HRBS and STEM-EELS results produced simulated results that adequately explain the contrast of the HAADF and HABF STEM images obtained at the interface. Consequently, our analysis of the atomic structure of amorphous-SiO_2/crystalline-Si including the *a*-Si layer clearly revealed that the random distribution of a crystalline material and amorphous material exists at the interface as a damaged layer formed by the low-energy oxygen bombardment.

ACKNOWLEDGMENTS

The authors thank T. Toyoda and K. Fujikawa of the Kobelko Research Institute, Inc. for help with SIMS and HRBS measurements. The authors express their appreciation to Kazuto Watanabe of the Tokyo Metropolitan College of Industrial Technology for his encouragement and guidance during this study.

*yamazakit@jp.fujitsu.com

[1] C. F. Yu, S. S. Todorov, and E. R. Fossum, J. Vac. Sci. Technol. A **5**, 1569 (1987).
[2] S. S. Todorov and E. R. Fossum, J. Vac. Sci. Technol. B **6**, 466 (1988).
[3] O. Vancauwenberghe, N. Herbots, and O. C. Hellman, J. Vac. Sci. Technol. A **10**, 713 (1992).
[4] O. Vancauwenberghe, O. Hellman, H. Herbots, W. Tan, J. Olson, and W. Croft, Mater. Sci. Eng. B **12**, 97 (1992).
[5] J. L. Alay and W. Vandervorst, Surf. Interface Anal. **19**, 313 (1992).
[6] S. S. Todorov and E. R. Fossum, Appl. Phys. Lett. **52**, 48 (1988).
[7] S. Todorov, I. Chakarov, and D. Karpuzov, Nucl. Instr. Meth. B **65**, 79 (1992).
[8] M. Watanabe and A. Tooi, Jpn. J. Appl. Phys. **5**, 737 (1966).
[9] E. Maydell-Ondrusz and I. Wilson, Thin Solid Films **114**, 357 (1984).
[10] Y. Homma and T. Maruo, Surf. Interface Anal. **14**, 725 (1989).
[11] C. J. Vriezema, K. T. F. Janssen, and P. R. Boudewijn, Appl. Phys. Lett. **54**, 1981 (1989).
[12] Y. Homma and K. Wittmaack, Appl. Phys. A **50**, 417 (1990).
[13] C. J. Vriezema and P. C. Zalm, Surf. Interface Anal. **17**, 875 (1991).
[14] J. S. Williams, M. Petravic, B. G. Svensson, and M. Conway, J. Appl. Phys. **76**, 1840 (1994).
[15] M. Petravic, B. G. Svensson, J. S. Williams, and J. M. Glasko, Nucl. Instr. Meth. B **118**, 151 (1996).
[16] K. Wittmaack, Philos. Trans. R. Soc. London A **354**, 2731 (1996).
[17] K. Wittmaack and S. F. Corcoran, J. Vac. Sci. Technol. B **16**, 272 (1998).
[18] C. W. Magee, G. R. Mount, S. P. Smith, B. Herner, and H.-J. Gossmann, J. Vac. Sci. Technol. B **16**, 3099 (1998).
[19] F. A. Stevie, P. M. Kahora, D. S. Simons, and P. Chi, J. Vac. Sci. Technol. A **6**, 76 (1988).
[20] K. Wittmaack, J. Vac. Sci. Technol. A **8**, 2246 (1990).
[21] Z. X. Jiang and P. F. A. Alkemade, J. Vac. Sci. Technol. B **16**, 1971 (1998).
[22] H. H. Hosack, M. K. El-Ghor, J. Hollingsworth, and K. Joyner, J. Appl. Phys. **73**, 1461 (1993).
[23] U. Bussmann and P. Hemment, Nucl. Instr. Meth. B **47**, 22 (1990).
[24] U. Bussmamnn, A. Robinson, and P. Hemment, Nucl. Instr. Meth. B **55**, 852 (1991).
[25] U. Bussmann and P. L. F. Hemment, Appl. Phys. Lett. **57**, 1200 (1990).
[26] L. Nesbit, G. Slusser, R. Frenette, and R. Holbach, J. Electrochem. Soc. **133**, 1186 (1986).
[27] J. Stoemenos, A. Garcia, B. Aspar, and J. Margail, J. Electrochem. Soc. **142**, 1248 (1995).
[28] S. Maeyama and K. Kajiyama, Jpn. J. Appl. Phys. **21**, 744 (1982).
[29] Y. P. Kim, S. K. Choi, H. K. Kim, and D. W. Moon, Appl. Phys. Lett. **71**, 3504 (1997).
[30] P. N. K. Deenapanray and M. Petravic, Surf. Interface Anal. **27**, 92 (1999).
[31] J. S. Williams, K. T. Short, M. Petravic, and B. G. Svensson, Nucl. Instr. Meth. B **121**, 24 (1997).

[32]S. D. Littlewood and J. A. Kilner, J. Appl. Phys. **63**, 2173 (1988).
[33]R. Chater, J. Kilner, K. Reeson, A. Robinson, and P. Hemment, Nucl. Instr. Meth. B **45**, 110 (1990).
[34]G. Beyer, S. Patel, and J. Kilner, Nucl. Instr. Meth. B **85**, 370 (1994).
[35]K. Wittmaack, Surf. Sci. **419**, 249 (1999).
[36]S. J. Pennycook and L. A. Boatner, Nature (London) **336**, 565 (1988).
[37]S. J. Pennycook and D. E. Jesson, Phys. Rev. Lett. **64**, 938 (1990).
[38]S. J. Pennycook and P. D. Nellist, *Impact of Electron and Scanning Probe Microscopy on Materials Research* (Kluwer, Dordrecht, 1999).
[39]E. J. Kirkland, R. F. Loane, and J. Silcox, Ultramicroscopy **23**, 77 (1987).
[40]S. C. Anderson, C. R. Birkeland, G. R. Anstis, and D. J. H. Cockayne, Ultramicroscopy **69**, 83 (1997).
[41]K. Watanabe, T. Yamazaki, Y. Kikuchi, Y. Kotaka, M. Kawasaki, I. Hashimoto, and M. Shiojiri, Phys. Rev. B **63**, 085316 (2001).
[42]J. M. LeBeau, S. D. Findlay, X. Wang, A. J. Jacobson, L. J. Allen, and S. Stemmer, Phys. Rev. B **79**, 214110 (2009).
[43]K. Kuramochi, Y. Kotaka, T. Yamazaki, M. Ohtsuka, I. Hashimoto, and K. Watanabe, Acta Crystallogr. Sect. A **66**, 10 (2009).
[44]M. Haider, S. Uhlemann, E. Schwan, H. Rose, B. Kabius, and K. Urban, Nature (London) **392**, 768 (1998).
[45]M. Haider, S. Uhlemann, and J. Zach, Ultramicroscopy **81**, 163 (2000).
[46]J. L. Hutchison, J. M. Titchmarsh, D. J. H. Cockayne, G. Mobus, C. J. Hetherington, R. C. Doole, F. Hosokawa, P. Hartel, and M. Haider, Proc. Microsc. Microanal. **8** (Suppl. S02), 10 (2002).
[47]H. Sawada, T. Tomita, M. Naruse, T. Honda, P. Hambridge, P. Hartel, M. Haider, C. Hetherington, R. Doole, A. Kirkland *et al.*, J. Electron Microsc. **54**, 119 (2005).
[48]T. Yamazaki, Y. Kotaka, M. Tsukada, and Y. Kataoka, Ultramicroscopy **110**, 1161 (2010).
[49]T. Yamazaki, Y. Kotaka, and Y. Kataoka, Ultramicroscopy **111**, 303 (2011).
[50]N. Nakanishi, Y. Kikuchi, T. Yamazaki, E. Okunishi, K. Watanabe, and I. Hashimoto, Phys. Rev. B **70**, 165324 (2004).
[51]Z. Yu, D. Muller, and J. Silcox, J. Appl. Phys. **95**, 3362 (2004).
[52]K. Watanabe, Y. Kikuchi, T. Yamazaki, E. Asano, N. Nakanishi, Y. Kotaka, E. Okunishi, and I. Hashimoto, Acta Crystallogr. Sect. A **60**, 591 (2004).
[53]T. Yamazaki, M. Kawasaki, K. Watanabe, I. Hashimoto, and M. Shiojiri, Ultramicroscopy **92**, 181 (2002).
[54]K. Kuramochi, T. Yamazaki, Y. Kotaka, M. Ohtsuka, I. Hashimoto, and K. Watanabe, Ultramicroscopy **110**, 36 (2009).
[55]R. F. Egerton, *Electron Energy-Loss Spectroscopy in the Electron Microscope*, 2nd ed. (Plenum Press, New York, 1996).
[56]J. M. LeBeau, S. D. Findlay, L. J. Allen, and S. Stemmer, Phys. Rev. Lett. **100**, 206101 (2008).
[57]K. Watanabe, T. Yamazaki, I. Hashimoto, and M. Shiojiri, Phys. Rev. B **64**, 115432 (2001).
[58]T. Yamazaki, K. Watanabe, K. Kuramochi, and I. Hashimoto, Acta Crystallogr. Sect. A **62**, 233 (2006).
[59]T. Yamazaki, K. Watanabe, N. Nakanishi, and I. Hashimoto, Ultramicroscopy **99**, 125 (2004).
[60]Q. Yang, D. OfConnor, and Z. Wang, Nucl. Instr. Meth. B **61**, 149 (1991).
[61]K. Kuramochi, K. Suzuki, T. Yamazaki, K. Mitsuishi, K. Furuya, I. Hashimoto, and K. Watanabe, Ultramicroscopy **109**, 96 (2008).
[62]T. Yamazaki, Y. Kotaka, T. Soeda, M. Ohtsuka, and K. Watanabe (in preparation).